

A physical model for the [C II]-FIR deficit in luminous galaxies

Desika Narayanan^{1*} & Mark R. Krumholz^{2,3}

¹*Department of Physics and Astronomy, Haverford College, 370 Lancaster Ave, Haverford, PA 19041*

²*Research School of Astronomy & Astrophysics, Australian National University, Canberra, ACT 2611, Australia*

³*Blaauw Visiting Professor, Kapteyn Astronomical Institute, University of Groningen, The Netherlands*

Submitted to MNRAS

ABSTRACT

Observations of ionised carbon at 158 μm ([C II]) from luminous star-forming galaxies at $z \sim 0$ show that their ratios of [C II] to far infrared (FIR) luminosity are systematically lower than those of more modestly star-forming galaxies. In this paper, we provide a theory for the origin of this so-called “[C II] deficit” in galaxies. Our model treats the interstellar medium as a collection of clouds with radially-stratified chemical and thermal properties, which are dictated by the clouds’ volume and surface densities, as well as the interstellar radiation and cosmic ray fields to which they are exposed. [C II] emission arises from the outer, H I-dominated layers of clouds, and from regions where the hydrogen is H_2 but the carbon is predominantly C^+ . In contrast, the most shielded regions of clouds are dominated by CO, and produce little [C II] emission. This provides a natural mechanism to explain the observed [C II]-star formation relation: galaxies’ star formation rates are largely driven by the surface densities of their clouds. As this rises, so does the fraction of gas in the CO-dominated phase that produces little [C II] emission. Our model further suggests that the apparent offset in the [C II]-FIR relation for high- z sources compared to those at present epoch may arise from systematically larger gas masses at early times: a galaxy with a large gas mass can sustain a high star formation rate even with a relatively modest surface density, allowing copious [C II] emission to coexist with rapid star formation.

Key words: astrochemistry — ISM: molecules — ISM: structure — galaxies: ISM

1 INTRODUCTION

The $^2P_{3/2} - ^2P_{1/2}$ fine structure transition of singly ionised carbon¹ (hereafter, [C II]) at $\lambda = 158 \mu\text{m}$ is one of the most luminous emission lines in star-forming galaxies, and a principal coolant of the neutral interstellar medium (ISM; Malhotra et al. 1997; Luhman et al. 1998; Nikola et al. 1998). Indeed, [C II] can account for $\sim 0.1 - 1\%$ of the far infrared (FIR) luminosity in galaxies (Stacey et al. 1991). The line is excited mainly via collisions with electrons, neutral hydrogen (H I), and molecular hydrogen (H_2), with the relatively low critical densities of ~ 44 , $\sim 3 \times 10^3$, and $\sim 6 \times 10^3 \text{ cm}^{-3}$ respectively (Goldsmith et al. 2012)². This, combined with the relatively low ionisation potential of 11.3 eV, means that [C II] emission can arise from nearly every phase in the ISM.

For present-epoch galaxies, ground-based observations of [C II] are challenging owing to telluric water vapor absorption in the Earth’s atmosphere. Early work with the Kuiper Airborne Observatory (KAO) and Infrared Space Observatory (ISO) presented evidence of a relationship between galaxies’ [C II] luminosities and their global star formation rates (SFRs). For example, KAO observations of 14 nearby galaxies by Stacey et al. (1991) revealed ratios of [C II]/ ^{12}CO ($J=1-0$) emission similar to those found Galactic star-forming regions, providing an indirect link between the [C II] line luminosity and SFR (via the $\Sigma_{\text{SFR}} - \Sigma_{\text{CO}}$ relation in galaxies). Later observations utilising ISO by Leech et al. (1999) and Boselli et al. (2002) established bona fide relations between [C II] and the SFR in $z \sim 0$ systems. More recently, the launch of the Herschel Space Observatory, combined with other high-resolution ultraviolet and infrared observations, have established a firm [C II]-SFR relation in nearby galaxies (de Looze et al. 2011; Sargsyan et al. 2012; Pineda et al. 2014; Herrera-Camus et al. 2015). Cosmological zoom simulations of galaxy formation by Olsen et al. (2015) have suggested that the majority of the [C II] emission that

* E-mail: dnarayan@haverford.edu

¹ Throughout this paper we will use [C II] when referring to the observable emission line, and C^+ when discussing ionised carbon within the context of chemical networks.

² At kinetic temperatures of 8000, 100 and 100 K, respectively.

drives this relationship originates in molecular gas or photodissociation regions (PDRs) in giant clouds, providing a natural explanation for why [C II] should be correlated with star formation.

This said, even since the early days of ISO observations of galaxies, it has been clear that the SFR-[C II] relationship breaks down in the $z \sim 0$ galaxies with the highest infrared luminosities. Put quantitatively, the [C II]/far infrared (FIR) luminosity ratio decreases with increasing infrared luminosity, such that ultraluminous infrared galaxies (ULIRGs; galaxies with $L_{\text{IR}} \geq 10^{12} L_{\odot}$) emit roughly $\sim 10\%$ of the [C II] luminosity that would be expected if they had the same [C II]/FIR ratios as galaxies of lower FIR luminosity (Malhotra et al. 1997, 2001; Luhman et al. 1998, 2003b). The evidence for the so-called “[C II]-FIR deficit” has grown stronger in the Herschel era. Graciá-Carpio et al. (2011) showed that the [C II]-FIR deficit is uncorrelated with galaxies’ nuclear activity level, and that similar deficits with respect to FIR luminosity may exist in other nebular lines as well. Díaz-Santos et al. (2013) added significantly to existing samples via a survey of [C II] emission from ~ 250 $z \sim 0$ luminous infrared galaxies (LIRGs; $L_{\text{IR}} \geq 10^{11} L_{\odot}$), and confirmed these conclusions. Other evidence for this deficit in local systems has come from Beirão et al. (2010), Croxall et al. (2012) and Farrah et al. (2013).

At high-redshift, the evidence for a [C II]-FIR deficit in galaxies is more mixed. While there have been a number of [C II] detections in $L_{\text{IR}} \geq 10^{12} L_{\odot}$ galaxies at $z \sim 2 - 6$ (see Casey, Narayanan & Cooray (2014) for a recent compendium of these data and review of high- z detections), and certainly many exhibit depressed [C II]/FIR luminosity ratios, many additionally show elevated [C II]/FIR luminosity ratios compared to local galaxies with a similar infrared luminosity (e.g. Iono et al. 2006; Stacey et al. 2010; Wagg et al. 2012; Swinbank et al. 2012; Rawle et al. 2013; Riechers et al. 2013; Wang et al. 2013; Rigopoulou et al. 2014; Brisbin et al. 2015).

In this paper, we aim to provide a physical explanation for the origin of the [C II]-FIR deficit in heavily star-forming galaxies in the local Universe, and the more complex pattern found at high redshift. We do this by developing analytic models for the structure of giant clouds in galaxies. We combine chemical equilibrium networks and numerical radiative transfer models with these cloud models to develop a picture for how [C II] emission varies both as a function of cloud radius, as well as with galactic environment.

Our central argument is relatively straight forward. Consider a galaxy with a two-phase neutral interstellar medium comprised of H₂ and H I. As the surface density of the gas in the galaxy grows, its star formation rate rises. However, the increased surface density also increases the ability of the hydrogen to shield itself from dissociating Lyman-Werner band photons (Krumholz et al. 2008, 2009a; McKee & Krumholz 2010), causing the H₂/H I ratio to rise. Within clouds, owing to cosmic ray and ultraviolet radiation-driven chemistry effects, C⁺ is prevalent in the photodissociation region but is significantly depleted in the H₂ core. As a result, the typical decreasing sizes of PDRs in galaxies of increasing star formation rate results in proportionally lower [C II] luminosities.

In what follows, we present a numerical model that shows these physical and chemical trends explicitly. In Sec-

tion 2 we describe the model, while in Section 3 we outline the main results, including the luminosities of [C II] in molecular and atomic gas. In Section 4 we discuss some applications of this model, including its utility for high-redshift galaxies and ISM calorimetry. We additionally discuss the relationship of our model to other theoretical models in this area, as well as uncertainties in our model. Finally, we summarise in Section 5.

2 MODEL DESCRIPTION

Our goal is to explain the observed relationship between [C II] 158 μm emission and star formation rate, for which FIR emission is a proxy. However, the physical state of a galaxy’s ISM obviously depends on more than its star formation rate. Quantities such as the volume density, chemical state, and temperature play a role as well. We therefore develop a minimal model for a galactic ISM as a whole, and then use that model to compute both SFR and [C II] emission.

We idealise a galaxy as a collection of spherical, virialised star-forming clouds. Each cloud consists of several radial zones that each have distinct column densities, and that are chemically and thermally independent from one another. To calculate the line emission from a galaxy, our first step is to compute the density, column density, and velocity dispersion of each of these clouds. We do so following the procedure outlined in Section 2.1. We then use the code Derive the Energetics and SPectra of Optically Thick Interstellar Clouds (DESPOTIC; Krumholz 2013a,b) to compute the chemical state (Section 2.2), temperature (Section 2.3), and level populations (Section 2.4) in every layer of the cloud. The entire model is iterated to convergence as outlined in Section 2.5, and, once convergence is reached, we can compute the total [C II] 158 μm luminosity.

For convenience, we have collected various parameters that appear in our model in Table 1.

2.1 Cloud Physical Structure

The chemical and thermal states of clouds, both in our model and in reality, will depend upon their volume and column densities, as well as their velocity dispersions. The first step in our calculation is therefore to model the relationship between these quantities and galaxies’ star formation rates. To this end, let Σ_g be the surface density of an idealised spherical cloud. The inner part of this cloud will be H₂-dominated and the outer layers, which are exposed to the unattenuated interstellar radiation field, will be dominated by H I; the specified surface density Σ_g includes both of these zones. The H₂-dominated region comprises a fraction f_{H_2} of the total cloud mass. Krumholz et al. (2008, 2009a,b) and McKee & Krumholz (2010) (hereafter collectively referred to as KMT) show that the molecular mass fraction for such a cloud obeys

$$f_{\text{H}_2} \approx 1 - \frac{3}{4} \frac{s}{1 + 0.25s} \quad (1)$$

for $s < 2$ and $f_{\text{H}_2} = 0$ for $s \geq 2$. Here $s = \ln(1 + 0.6\chi + 0.01\chi^2)/(0.6\tau_c)$, where $\chi = 0.76(1 + 3.1Z^{0.365})$, the dust optical depth of the cloud at frequencies in the Lyman-Werner

Table 1. Parameters used in cloud models

Variable	Definition	Value
Parameters for Cloud Physical Properties (Section 2.1)		
ϵ_{ff}	Dimensionless star formation efficiency	0.01
α_{vir}	Cloud virial ratio	1.0
ρ_{MW}	Molecular cloud density normalisation	$2.34 \times 10^{-22} \text{ g cm}^{-3}$
N	Star formation law index	2
ϕ_{mol}	Ratio of molecular to atomic density	10
M_{gal}	Galaxy gas mass	$1 \times 10^9 - 2 \times 10^{11} M_{\odot}$
Σ_g	Cloud surface density	$\sim 50 - 5000 M_{\odot} \text{ pc}^{-2}$
Parameters for Cloud Thermal and Chemical Properties		
N_{zones}	Number of radial zones in model clouds	16
χ_{FUV}	FUV ISRF	$1.0 \times \text{SFR}/(M_{\odot} \text{ yr}^{-1})$
ζ_{-16}	cosmic ray ionisation rate	$0.1 \times \text{SFR}/(M_{\odot} \text{ yr}^{-1})$
α_{GD}	gas-dust coupling coefficient	$3.2 \times 10^{-34} \text{ erg cm}^3 \text{ K}^{-3/2}$
$\sigma_{\text{d},10}$	dust cross-section to 10 K thermal radiation	$2.0 \times 10^{-26} \text{ cm}^2 \text{ H}^{-1}$
T_{CMB}	CMB temperature	2.73 K
Z'_{d}	dust abundance relative to solar	1
β_{d}	dust opacity versus frequency index	2
A_V/N_H	visual extinction per column	$4 \times 10^{-22} Z' \text{ mag cm}^2$
OPR	ortho to para ratio in H ₂ gas	0.25

band is $\tau_c = 0.066 \Sigma_g / (M_{\odot} \text{ pc}^{-2}) \times Z'$, and Z' is the metallicity normalised to the solar metallicity. We assume $Z' = 1$ for all model clouds, and thus f_{H_2} is a function of Σ_g alone.

We relate the atomic and molecular regions via their density contrast. Specifically, following KMT we define

$$\phi_{\text{mol}} = \frac{\rho_{\text{H}_2}}{\rho_{\text{HI}}}, \quad (2)$$

where ρ_{H_2} and ρ_{HI} are the densities in the molecular atomic zones, respectively, and we adopt a fiducial value $\phi_{\text{mol}} = 10$ based on observations. With this choice and a bit of algebra, one can show that the total cloud mass and radius can be expressed in terms of Σ_g and ρ_{H_2} as

$$M_c = \frac{9}{16} \pi [f_{\text{H}_2} + \phi_{\text{mol}}(1 - f_{\text{H}_2})]^2 \frac{\Sigma_g^3}{\rho_{\text{H}_2}^2} \quad (3)$$

$$R_c = \frac{3}{4} \left(1 + \phi_{\text{mol}} \frac{1 - f_{\text{H}_2}}{f_{\text{H}_2}} \right) \frac{\Sigma_g}{\rho_{\text{H}_2}}. \quad (4)$$

We can also express the velocity dispersion of the cloud in terms of these two variables via the virial theorem. Specifically, we have (Bertoldi & McKee 1992)

$$\alpha_{\text{vir}} = \frac{5\sigma_c^2 R_c}{GM_c} \quad (5)$$

where σ_c is the velocity dispersion and α_{vir} is the virial ratio. Thus

$$\sigma_c = \sqrt{\frac{3\pi}{20} \alpha_{\text{vir}} f_{\text{H}_2}^2 \left(1 + \phi_{\text{mol}} \frac{1 - f_{\text{H}_2}}{f_{\text{H}_2}} \right) \frac{G \Sigma_g^2}{\rho_{\text{H}_2}}} \quad (6)$$

We adopt a fiducial value for the virial ratio $\alpha_{\text{vir}} = 1$, typical of observed molecular clouds (e.g. Dobbs et al. 2011, 2013; Heyer & Dame 2015). Recalling that f_{H_2} is a function of Σ_g alone, we have now succeeded in writing the cloud mass, radius, and velocity dispersion in terms of Σ_g and ρ_{H_2} alone, and we have therefore reduced our model to a two-parameter family.

To proceed further, we now bring star formation into the picture. Consider a galaxy with a total ISM mass $M_{\text{gal}} = N_c M_c$, where N_c is the number of star-forming clouds in the galaxy. At all but the lowest metallicities, stars form only in the molecular region of the ISM (e.g., Krumholz et al. 2011; Glover & Mac Low 2011; Krumholz 2012). Thus the total star formation rate of the galaxy is given by

$$\text{SFR} = \epsilon_{\text{ff}} \frac{f_{\text{H}_2} M_{\text{gal}}}{t_{\text{ff}}}, \quad (7)$$

where t_{ff} is the free-fall time, and given by

$$t_{\text{ff}} = \sqrt{\frac{3\pi}{32G\rho_{\text{H}_2}}}, \quad (8)$$

and the quantity ϵ_{ff} is the fraction of the molecular mass converted to stars per free-fall time. Observations strongly constrain this to be within a factor of a few of 1% (Krumholz & Tan 2007; Krumholz et al. 2012; Krumholz 2014), so we adopt $\epsilon_{\text{ff}} = 0.01$ as a fiducial value.

Since f_{H_2} is a function of Σ_g alone in our model, we now have the star formation rate in terms of three parameters: Σ_g , M_{gal} , and ρ_{H_2} . We can eliminate the last of these on empirical grounds. The Milky Way has $\Sigma_g \approx 100 M_{\odot} \text{ pc}^{-2}$ and $\rho_{\text{H}_2} \approx 100 \mu_{\text{H}} \text{ cm}^{-3}$, where $\mu_{\text{H}} = 2.34 \times 10^{-24} \text{ g}$ is the mean mass per H nucleus for gas that is 90% H and 10% He by mass (Dobbs et al. 2014; Heyer & Dame 2015). The remaining question is how ρ_{H_2} scales as we vary Σ_g ; we assume that it does not vary with M_{gal} at fixed Σ_g , since variations of this form correspond simply to a galaxy having a smaller or larger star-forming disk. To derive this relationship, we note that observations of galaxies over a large range in surface densities show that the SFR surface density is well-correlated with the gas surface density (Kennicutt & Evans 2012), $\Sigma_{\text{SFR}} \propto \Sigma_g^N$, when the star formation rate and gas surface densities measured over $\sim 1 \text{ kpc}$ scales. The exact value of the index N is debated in the literature,

and is dependent on the exact sample, fitting method, and the value assumed to convert CO line luminosity (the most common method used to measure Σ_g in extragalactic observations) to H₂ gas mass (Bigiel et al. 2008; Blanc et al. 2009; Narayanan et al. 2011a,b, 2012a; Shetty et al. 2013a,b). We adopt a fiducial value $N = 2$, motivated by theoretical studies that suggest such a relation for LIRGs and ULIRGs when considering a CO-H₂ conversion factor that varies with ISM physical conditions (Narayanan et al. 2012a). Since we also have $\Sigma_{\text{SFR}} \propto \Sigma_g/t_{\text{ff}}$, we immediately have $t_{\text{ff}} \propto \Sigma_g^{1-N}$, and thus $\rho_{\text{H}_2} \propto \Sigma_g^{2(N-1)}$. Combining this scaling with the Milky Way normalisation described above, we arrive at our fiducial scaling between ρ_{H_2} and Σ_g :

$$\rho_{\text{H}_2} = \rho_{\text{MW}} \left(\frac{\Sigma_g}{100 M_{\odot} \text{ pc}^{-2}} \right)^{2(N-1)} \quad (9)$$

with $\rho_{\text{MW}} = 100\mu_{\text{H}}$ and $N = 2$. We discuss how changing either of the coefficient or index of this relation would affect our results in Section 4.5. However, we note that this scaling produces reasonable values for the Milky Way: the ISM mass inside the Solar Circle is $M_{\text{gal}} \approx 2 \times 10^9 M_{\odot}$ considering both H I (Wolfire et al. 2003) and H₂ (Heyer & Dame 2015), and using $\Sigma_g = 100 M_{\odot} \text{ pc}^{-2}$ in equation 7 gives a total star formation rate of $3.7 M_{\odot} \text{ yr}^{-1}$, within a factor of a few of the consensus range of $1 - 2 M_{\odot} \text{ yr}^{-1}$ derived by Robitaille & Whitney (2010) and Chomiuk & Povich (2011).

We have therefore succeeded in completely specifying our model for the physical structure of star-forming galaxies and the clouds within them in terms of two free parameters, Σ_g and M_{gal} . We take to the former be in the range $\log \Sigma_g \in [1.75, 3.75] M_{\odot} \text{ pc}^{-2}$, and the latter to be in the range $M_{\text{gal}} = 10^9 - 10^{10} M_{\odot}$ for local galaxies, and $\sim 10^{10} - 10^{11} M_{\odot}$ for high redshift ones. The minimum in the surface densities is motivated by observations of nearby galaxies (e.g. Bolatto et al. 2008; Leroy et al. 2013), while the range in galaxy gas masses is constrained by surveys of galaxies near and far (Saintonge et al. 2011; Bothwell et al. 2013).

Finally, we convert between star formation rate and observed infrared luminosity employing the Murphy et al. (2011) conversion as summarised by Kennicutt & Evans (2012),

$$\log_{10}(L_{\text{IR}}(3 - 1100 \mu\text{m})) = \log_{10}(\text{SFR}) + 43.41. \quad (10)$$

2.2 Chemical Structure

As mentioned above, our clouds consist of radial layers, each chemically independent from one another. Each cloud contains N_{zone} zones, with a default $N_{\text{zone}} = 16$. We show in § A that this is sufficient to produce a converged result. We assign each cloud a center-to-edge column density of H nuclei $N_{\text{H}} = (3/4)\Sigma_g/\mu_{\text{H}}$; the factor of (3/4) is simply the difference between the mean column density and the center-to-edge column density. In this model, we assign the i th zone (starting with $i = 0$) to cover the range of column densities from $[i/N_{\text{zone}}]N_{\text{H}}$ to $[(i+1)/N_{\text{zone}}]N_{\text{H}}$, with a mean column density $N_{\text{H},i} = [(i+1/2)/N_{\text{zone}}]N_{\text{H}}$. We calculate the mass in each zone from the column density range and the volume density, assuming spherical geometry.

In each zone we must determine the chemical state of

the carbon and oxygen atoms. These two species, either separately in atomic form or combined into CO, are the dominant coolants and line emitters. We adopt total abundances of $[\text{C}/\text{H}] = 2 \times 10^{-4}$ and $[\text{O}/\text{H}] = 4 \times 10^{-4}$ for C and O, respectively, consistent with their abundances in the Milky Way (Draine 2011). In principle, depending on the physical properties of the gas in each layer, the carbon can be stored predominantly as C⁺, C, or CO. Similarly, the hydrogen can be in atomic or molecular form in any given layer, and this chemical state of the H in turn affects that of the C and O. To model these effects, we compute the chemical state of each zone using the reduced carbon-oxygen chemical network developed by Nelson & Langer (1999) combined with the Glover & Mac Low (2007) non-equilibrium hydrogen chemical network,³ combined following the procedure described in Glover & Clark (2012). We summarise the reactions included in our network, and the rate coefficients we use for them, in Table 2. We refer readers to Glover & Clark (2012) for full details on the network and its implementation, but we mention here three choices that are specific to the model we use in this paper.

First, the network requires that we specify the strength of the unshielded interstellar radiation field (ISRF). We characterise this in terms of the FUV radiation intensity normalised to the Solar neighborhood value, χ_{FUV} . We assume that χ_{FUV} is proportional to a galaxy's SFR normalised to the $1 M_{\odot} \text{ yr}^{-1}$ SFR of the Milky Way (Robitaille & Whitney 2010; Chomiuk & Povich 2011): $\chi_{\text{FUV}} = \text{SFR}/(M_{\odot} \text{ yr}^{-1})$.

Second, we must compute the amount by which all photochemical reaction rates are reduced in the interiors of clouds by shielding of the ISRF. The DESPOTIC implementation of the Glover & Clark (2012) network that we use includes reductions in the rates of all photochemical reactions by dust shielding, and reductions in the rates of H₂ and CO dissociation by self-shielding and (for CO) H₂ cross shielding. We characterise dust shielding in terms of the visual extinction $A_V = (1/2)(A_V/N_{\text{H}})N_{\text{H}}$, where the ratio (A_V/N_{H}) is the dust extinction per H nucleus at V band (Table 1). The factor of (1/2) gives a rough average column density over the volume of the cloud. We evaluate the reduction in the H₂ dissociation rate using the shielding function of Draine & Bertoldi (1996), which is a function of the H₂ column density and velocity dispersion; for the latter we use the value given by equation 6, while for the former we use $N_{\text{H}_2} = x_{\text{H}_2}N_{\text{H}}$, where x_{H_2} is the abundance of H₂ molecules

³ By using the Glover & Mac Low (2007) model for hydrogen chemistry, we are folding an inconsistency into our model. Specifically, to determine the bulk physical properties of our model clouds, including the star formation rates, we utilise the KMT model to decompose the ISM phases into neutral hydrogen and molecular. This is unavoidable as the networks require knowledge of the background radiation field and cosmic ray ionisation rate, both of which likely depend on the star formation rate and thus the H₂ fraction. To be fully consistent we would be required to iterate between chemistry and star formation, which would be quite computationally expensive. Hereafter in the paper, all hydrogen phase abundances that we quote derive from what is explicitly calculated in the chemical equilibrium network. However, the level of inconsistency is generally small, in that the H₂ fraction that results from the explicit chemical modeling never deviates that strongly from the KMT prediction, varying by a maximum of a factor of ~ 2 within the surface density range of interest.

Table 2. Coefficients adopted for our chemical network, following Glover & Clark (2012). In this table, ζ is the cosmic ray primary ionisation rate, χ_{FUV} is the normalized FUV radiation field strength, A_V is the visual extinction, $x_{\text{H}} = n_{\text{H}}/n$ is the H abundance, $x_{\text{H}_2} = n_{\text{H}_2}/n$ is the H₂ abundance, $T_4 = T/(10^4 \text{ K})$, $\ln(T_e) = \ln(8.6173 \times 10^{-5} \times T/\text{K})$. Note that this network includes several super-species: CH_x agglomerates CH, CH₂, etc., and similarly for OH_x, and M and M⁺ agglomerate a number of metallic species with low ionisation potentials (e.g., Fe, Si).

Reaction	Rate Coefficient
Cosmic Ray Reactions [s ⁻¹ molecule ⁻¹]:	
cr + H → H ⁺ + e	ζ
cr + H ₂ → H ₃ ⁺ + e + H + cr	2ζ
cr + He → He ⁺ + e + cr	1.1ζ
Photoreactions [s ⁻¹ molecule ⁻¹]:	
$\gamma + \text{H}_2 \rightarrow 2 \text{H}$	$5.6 \times 10^{-11} \chi_{\text{FUV}} f_{\text{shield}}(N_{\text{H}_2}) e^{-3.74 A_V}$
$\gamma + \text{CO} \rightarrow \text{C} + \text{O}$	$2 \times 10^{-10} \chi_{\text{FUV}} f_{\text{shield}}(N_{\text{CO}}, N_{\text{H}_2}) e^{-3.53 A_V}$
$\gamma + \text{C} \rightarrow \text{C}^+ + \text{e}$	$3 \times 10^{-10} \chi_{\text{FUV}} e^{-3 A_V}$
$\gamma + \text{CH}_x \rightarrow \text{C} + \text{H}$	$1 \times 10^{-9} \chi_{\text{FUV}} e^{-1.5 A_V}$
$\gamma + \text{OH}_x \rightarrow \text{O} + \text{H}$	$5 \times 10^{-10} \chi_{\text{FUV}} e^{-1.7 A_V}$
$\gamma + \text{M} \rightarrow \text{M}^+ + \text{e}$	$3.4 \times 10^{-10} \chi_{\text{FUV}} e^{-1.9 A_V}$
$\gamma + \text{HCO}^+ \rightarrow \text{CO} + \text{H}$	$1.5 \times 10^{-10} \chi_{\text{FUV}} e^{-2.5 A_V}$
Ion-Neutral Reactions [cm ³ s ⁻¹ molecule ⁻¹]:	
H ₃ ⁺ + CI → CH _x + H ₂	2×10^{-9}
H ₃ ⁺ + OI → OH _x + H ₂	8×10^{-10}
H ₃ ⁺ + CO → HCO ⁺ + H ₂	1.7×10^{-9}
He ⁺ + H ₂ → He + H + H ⁺	7×10^{-15}
He ⁺ + CO → C ⁺ + O + He	$1.4 \times 10^{-9} / \sqrt{T/300}$
C ⁺ + H ₂ → CH _x + H	4×10^{-16}
C ⁺ + OH _x → HCO ⁺	1×10^{-9}
Neutral-Neutral Reactions [cm ³ s ⁻¹ molecule ⁻¹]:	
OI + CH _x → CO + H	2×10^{-10}
CI + OH _x → CO + H	$5 \times 10^{-12} \sqrt{T}$
Recombinations and Charge-Transfers [cm ³ s ⁻¹ molecule ⁻¹]:	
He ⁺ + e → He + γ	$1 \times 10^{-11} / \sqrt{T} \times (11.19 - 1.676 \times \log_{10}(T) - 0.2852 \times \log_{10}(T^2) + 0.04433 \times \log_{10}(T^3))$
H ₃ ⁺ + e → H ₂ + H	$2.34 \times 10^{-8} (T/300)^{-0.52}$
H ₃ ⁺ + e → 3H	$4.36 \times 10^{-8} (T/300)^{-0.52}$
C ⁺ + e → CI + γ	$4.67 \times 10^{-12} (T/300)^{-0.6}$
HCO ⁺ + e → CO + H	$2.76 \times 10^{-7} (T/300)^{-0.64}$
M ⁺ + e → M + γ	$3.8 \times 10^{-10} T^{-0.65}$
H ₃ ⁺ + M → M + γ	2×10^{-9}
Hydrogenic Chemistry [cm ³ s ⁻¹ molecule ⁻¹]:	
H ⁺ + e → H	$2.753 \times 10^{-14} \times (315614/T)^{1.5} \times (1 + (115188/T)^{0.407})^{-2.242}$
H ₂ + H → 3H	$k_{\text{H},1} = 6.67 \times 10^{-12} \sqrt{T} \times e^{-(1.0 + \frac{63590}{T})}$ $k_{\text{H},h} = 3.52 \times 10^{-9} e^{-\frac{43900}{T}}$ $n_{\text{cr},\text{H}} = 10^{(3 - 0.416 \times \log_{10} T_4 - 0.327 \times (\log_{10}(T_4))^2)}$ $n_{\text{cr},\text{H}_2} = 10^{(4.845 - 1.3 \times \log_{10}(T_4) + 1.62 \times (\log_{10}(T_4))^2)}$ $n_{\text{cr}} = (x_{\text{H}}/n_{\text{cr},\text{H}} + x_{\text{H}_2}/n_{\text{cr},\text{H}_2})^{-1}$ $\exp[(n/n_{\text{cr}})/(1. + n/n_{\text{cr}}) \times \log_{10}(k_{\text{H},h}) + 1/(1 + n/n_{\text{cr}}) \times \log_{10}(k_{\text{H},1})]$
H ₂ + H ₂ → H ₂ + 2H	$k_{\text{H}_2,1} = 5.996 \times 10^{-30} T^{4.1881} / (1 + 6.761 \times 10^{-6} \times T)^{(5.6881)} \times e^{-54657.4/T}$ $k_{\text{H}_2,h} = 1.9 \times 10^{-9} \times e^{-53300/T}$ $\exp[(n/n_{\text{cr}})/(1. + (n/n_{\text{cr}})) \times \log_{10}(k_{\text{H}_2,h}) + 1/(1 + n/n_{\text{cr}}) \times \log_{10}(k_{\text{H}_2,1})]$
H + e → H ⁺ + 2e	$\exp[-37.7 + 13.5 \times \ln(T_e) - 5.7 \times \ln(T_e)^2 + 1.6 \times \ln(T_e)^3 - 0.28 \times \ln(T_e)^4 + 0.03 \times \ln(T_e)^5 - 2.6 \times \ln(T_e)^6 + 1.1 \times \ln(T_e)^7 - 2.0 \times \ln(T_e)^8]$
He ⁺ + H ₂ → H ⁺ + He + H	$3.74 \times 10^{-14} e^{-35/T}$
H + H + grain → H ₂ + grain	$f_A = 1/(1 + 10^4 \times e^{-600/T_d})$ $3 \times 10^{-18} \sqrt{T} * f_A / (1 + 0.04 * \sqrt{T + T_d} + 0.002T + 8 \times 10^{-6} \times \sqrt{T})$
H ⁺ + e + grain → H + grain	$\psi = \chi \sqrt{T} / n_e$ $12.25 \times 10^{-14} / (1 + 8 \times 10^{-6} \psi^{1.378} (1 + 508 \times T^{0.016} \psi^{-0.47 - 1.1 \times 10^{-5} \ln(T)}))$

per H nucleus in the zone in question; note that each zone is independent, so we do not use information on the chemical composition of outer zones to evaluate x_{H_2} , a minor inconsistency in our model. Similarly, we compute the reduction in the CO photodissociation rate using an interpolated version of the shielding function tabulated by [van Dishoeck & Black \(1988\)](#), which depends on the CO and H₂ column densities. We evaluate the CO column density as $N_{\text{CO}} = x_{\text{CO}}N_{\text{H}}$, in analogy with our treatment of the H₂ column. We determine both abundances x_{H_2} and x_{CO} by iterating the network to convergence – see [Section 2.5](#).

Third, we must also specify the cosmic ray primary ionisation rate ζ . The value of this parameter even in the Milky Way is significantly uncertain. Recent observations suggest a value $\zeta \sim 10^{-16} \text{ s}^{-1}$ in the diffuse ISM ([Neufeld et al. 2010](#); [Indriolo et al. 2012](#)), but if a significant amount of the cosmic ray flux is at low energies, the ionisation rate in the interiors of molecular clouds will be lower due to shielding; indeed, a rate as high as 10^{-16} s^{-1} appears difficult to reconcile with the observed low temperatures of $\sim 10 \text{ K}$ typically found in molecular gas ([Narayanan et al. 2012a](#); [Narayanan & Davé 2012](#)). For this reason, we adopt a more conservative value of $\zeta = 10^{-17} \text{ s}^{-1}$ as our fiducial choice for the Milky Way. We discuss how this choice influences our results in [Section 4.3](#). We further assume that the cosmic ray ionisation rate scales linearly with the total star formation rate of a galaxy, so our final scaling is $\zeta_{-16} = 0.1 \times \text{SFR}/(M_{\odot} \text{ yr}^{-1})$, where $\zeta_{-16} \equiv \zeta/10^{-16} \text{ s}^{-1}$. Note that this choice of scaling too is significantly uncertain, and others are plausible.⁴

2.3 Thermal State of Clouds

The third component of our model is a calculation of the gas temperature, which we compute independently for each zone of our model clouds. We find the temperature by balancing the relevant heating and cooling processes, as well as energy exchange with dust. Following [Goldsmith \(2001\)](#), the processes we consider are photoelectric and cosmic ray heating of the gas, line cooling of the gas by C⁺, C, O, and CO, heating of the dust by the ISRF and by a thermal infrared field, cooling of the dust by thermal emission, and collisional exchange between the dust and gas. We also include cooling by atomic hydrogen excited by electrons via the Lyman α and Lyman β lines and the two-photon continuum, using interpolated collisional excitation rate coefficients ([Osterbrock & Ferland 2006](#), Table 3.16); these processes become important at temperatures above $\sim 5000 \text{ K}$, which are sometimes reached in the outer zones of our clouds. Formally,

$$\Gamma_{\text{pe}} + \Gamma_{\text{CR}} - \Lambda_{\text{line}} - \Lambda_{\text{H}} + \Psi_{\text{gd}} = 0 \quad (11)$$

$$\Gamma_{\text{ISRF}} + \Gamma_{\text{thermal}} - \Lambda_{\text{thermal}} - \Psi_{\text{gd}} = 0. \quad (12)$$

Terms denoted by Γ are heating terms, those denoted by Λ are cooling terms, while the gas-dust energy exchange term

⁴ For example, [Papadopoulos \(2010\)](#) and [Bisbas et al. \(2015\)](#) assume that cosmic ray intensity scales as the volume density of star formation rather than the total rate of star formation; which assumption is closer to reality depends on the extent to which cosmic rays are confined by magnetic fields and subject to losses as they propagate through a galaxy.

Ψ_{gd} can have either sign depending on the gas-dust temperature difference; our convention is that a positive sign corresponds to dust being hotter than the gas, leading to a transfer from dust to gas.

As with the chemical calculation, we solve these equations using the DESPOTIC code, and we refer readers to [Krumholz \(2013a\)](#) for a full description of how the rates for each of these processes are computed. The parameters we adopt are as shown in [Table 1](#). Note that the line cooling rate depends on the statistical equilibrium calculated as described in [Section 2.4](#).

2.4 Statistical Equilibrium

The final part of our model is statistical equilibrium within the level populations of each species. The DESPOTIC code computes these using the escape probability approximation for the radiative transfer problem. Formally we determine the fraction f_i of each species in quantum state i by solving the linear system

$$\begin{aligned} \sum_j f_j \left[q_{ji} + \beta_{ji}(1 + n_{\gamma,ji})A_{ji} + \beta_{ij} \frac{g_i}{g_j} n_{\gamma,ij} A_{ij} \right] \\ = f_i \sum_k \left[q_{ik} + \beta_{ik}(1 + n_{\gamma,ik})A_{ik} + \beta_{ki} \frac{g_k}{g_i} n_{\gamma,ki} A_{ki} \right] \end{aligned} \quad (13)$$

subject to the constraint $\sum_i f_i = 1$. Here A_{ij} is the Einstein coefficient for spontaneous transitions from state i to state j , g_i and g_j are the degeneracies of the states,

$$n_{\gamma,ij} = \frac{1}{\exp(\Delta E_{ij}/k_B T_{\text{CMB}}) - 1} \quad (14)$$

is the photon occupation number of the cosmic microwave background at the frequency corresponding to the transition between the states, E_{ij} is the energy difference between the states, and β_{ij} is the escape probability for photons of this energy. We compute the escape probability for each shell independently, assuming a spherical geometry. The escape probabilities computed include the effects of both resonant and dust absorption – see [Krumholz \(2013a\)](#) for details. Finally, q_{ij} is the collisional transition rate between the states, which is given by $q_{ij} = f_{\text{cl}} n_{\text{H}} k_{\text{H},ij}$ or $q_{ij} = f_{\text{cl}} n_{\text{H}_2} k_{\text{H}_2,ij}$ in the H I and H₂ regions, respectively; the quantities $k_{\text{H},ij}$ and $k_{\text{H}_2,ij}$ are the collision rate coefficients, n_{H} and n_{H_2} are the number densities of H atoms or H₂ molecules, and f_{cl} is a factor that accounts for the enhancement in collision rates induced by turbulent clumping.

All the Einstein coefficients and collisional rate coefficients required for our calculation come from the Leiden Atomic and Molecular Database ([Schöier et al. 2005](#)). In particular, we make use of the following collision rate coefficients: C⁺ with H ([Launay & Roueff 1977](#); [Barinovs et al. 2005](#)), C⁺ with H₂ ([Lique et al. 2013](#); [Wiesenfeld & Goldsmith 2014](#)), C with H ([Launay & Roueff 1977](#)), C with He ([Staemmler & Flower 1991](#)), C with H₂ ([Schroder et al. 1991](#)), O with H ([Abrahamsson et al. 2007](#)), O with H₂ ([Jaquet et al. 1992](#)), and CO with H₂ ([Yang et al. 2010](#)).

2.5 Convergence and Computation of the Emergent Luminosity

Calculation of the full model proceeds via the following steps. First, we compute the physical properties of each cloud following the method given in Section 2.1. Armed with these, we guess an initial temperature, chemical state, and set of level populations for each layer in the cloud. We then perform a triple-iteration procedure, independently for each zone. The outermost loop is to run the chemical network (Section 2.2) to convergence while holding the temperature fixed. The middle loop is to compute the temperature holding the level populations fixed (Section 2.3). The innermost loop is to iterate the level populations of each species to convergence (Section 2.4). We iterate in this manner until all three quantities – chemical abundances, temperature, and level populations – remain fixed to within a certain tolerance, at which point we have found a consistent chemical, thermal, and statistical state for each zone.

Once the level populations are in hand, it is straightforward to compute the observable luminosity in the [C II] 158 μm line, or in any other transition. The total luminosity per unit mass produced in a line produced by molecules or atoms of species S transitioning between states i and j , summed over each zone, is

$$L_{ij}/M = \mu_{\text{H}}^{-1} x_S \beta_{ij} \left[(1 + n_{\gamma,ij}) f_i - \frac{g_i}{g_j} n_{\gamma,ij} f_j \right] A_{ij} E_{ij}, \quad (15)$$

where x_S is the abundance of the species and f_i and β_{ij} are the level populations and escape probabilities in each layer. Each zone n has a mass M_n , computed from its range of column densities, and the total luminosity of the N_c clouds in the entire galaxy is simply

$$L_{ij} = N_c \mu_{\text{H}}^{-1} A_{ij} E_{ij} \sum_n M_n x_{S,n} \beta_{ij,n} \cdot \left[(1 + n_{\gamma,ij}) f_{i,n} - \frac{g_i}{g_j} n_{\gamma,ij} f_{j,n} \right], \quad (16)$$

where $x_{S,n}$, $f_{i,n}$, and $\beta_{ij,n}$ are the abundance, level population fraction, and escape probability in the n th zone of our model clouds.

2.6 Sample Results

Before moving on to our results for [C II] emission, in this section we provide a brief example of the thermal and chemical properties that our models produce. These will provide the reader with some intuition for how the physical, thermal, and chemical properties of our model clouds vary with galaxy infrared luminosity, or mean cloud surface density. For this example, we consider a galaxy with a gas mass of $M_{\text{gas}} = 10^9 M_{\odot}$ (i.e. similar to the Milky Way), and we vary the surface density Σ_g within the range specified in Table 1. For each value of Σ_g we derive a star formation rate (equation 7) and thus a far infrared luminosity, and we run the chemical-thermal-statistical network to equilibrium following the procedure described in Section 2.5. We summarise the resulting cloud properties as a function of FIR luminosity and Σ_g in Figure 1, where we show the cloud mean densities, fractional chemical abundances for a few species, gas kinetic temperatures, and ISM heating/cooling rates as a function of cloud surface density (and galaxy infrared luminosity).

The fractional abundance subpanels of Figure 1 summarise the central arguments laid out in this paper. As the total cloud surface densities rise, so does the typical mass fraction of gas in the H_2 phase (Krumholz et al. 2008), owing to the increased ability of hydrogen to self-shield against dissociating Lyman-Werner band photons. This point is especially pertinent to our central argument. At a fixed galaxy mass, increased gas surface densities lead to increased star formation rates. In these conditions, the molecular to atomic ratio in giant clouds increases. At the same time, with increasing cloud surface density (or galaxy star formation rate), C^+ abundances decline, and CO abundances increase. This owes principally to the role of dust column shielding CO from photodissociating radiation. The fraction of the cloud that is dominated by C^+ hence decreases with increasing cloud surface density.

For the temperature, we discriminate between H_2 and H I gas in clouds, and plot the mass-weighted values for each phase. We additionally show the CO luminosity-weighted gas temperature with the dashed line, as this is the temperature that most closely corresponds to observations. At low cloud surface densities, the CO dominates the cool ($T \sim 15$ K) inner parts of clouds, though the warmer outer layers are dominated by C I and C^+ . The bulk of the mass is at these warmer temperatures, and the heating is dominated by the grain photoelectric effect. At higher cloud surface densities, the bulk of the cloud is dominated by CO. Here, the grain photoelectric effect is less effective owing to increased A_V , but the impact of cosmic ray ionisations and energy exchange with dust is increased.

3 RESULTS

In the model that we develop, the [C II]-FIR deficit in galaxies principally owes to a combination of atomic PDRs serving as the dominant site of C^+ in galaxies, and a decreasing atomic to molecular fraction in galaxies of increasing luminosity. In this section, we lay the case for this argument in detail.

3.1 Carbon-based Chemistry

We begin with the instructive question: how is CO in clouds typically formed and destroyed? The principle formation channels for CO are via neutral-neutral reactions with CH_x and OH_x . CO is destroyed in the ISM via both cosmic rays and ultraviolet radiation. The molecule is directly destroyed most efficiently via interactions with ionised helium, He^+ , which is created via cosmic ray ionisations of neutral He. At the same time, FUV radiation can also reduce CO abundances via a variety of channels: it can directly destroy CO, as well as prevent its formation via the photodissociation of CO's main formation reactants, C I , CH_x , and OH_x . Once carbon is in neutral atomic form, UV radiation can ionise C I in order to form C^+ .

Opposing CO dissociation and ionisation (and consequently the formation of C^+) are the surface density and volumetric density of the cloud. To understand the role of the surface density, consider the photo-reactions in Table 2. The dissociation rates are only linearly dependent on the ultraviolet radiation field strength, but exponentially decrease

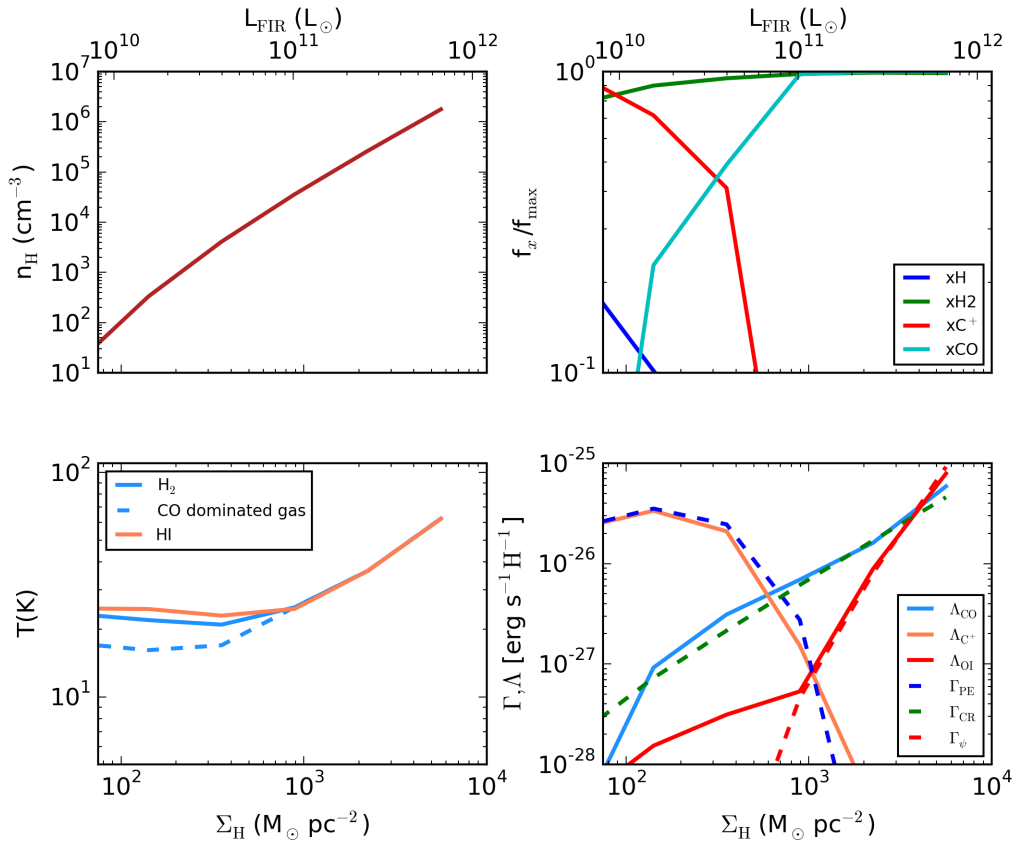


Figure 1. Physical properties of model clouds inside a galaxy of $M_{\text{gas}} = 10^9 M_\odot$ as a function of cloud surface density. These include volume density (top left), chemical abundances (top right), gas kinetic temperature (bottom left), and heating/cooling rates (bottom right). All quantities shown are mass-weighted averages, with the exception that in the gas kinetic temperature panel the different lines correspond to temperatures weighted by H I mass, H₂ mass, and CO luminosity, respectively.

with increased A_V . In particular, increased surface densities prevent the dissociation and ionisation of CH_x, OH_x, and CO molecules, as well as C I.

Increased volumetric densities, n_H , also promote neutral atom and molecule formation, and prevent the formation of C⁺. Again, consider the photoionisation of neutral carbon. The reaction rates for photodissociations and photoionisations are density-independent. However, the recombination and molecular formation rates within the ion-molecule, ion-atom and neutral-neutral reactions all scale linearly with density. Hence, given sufficient density, recombination and molecule formation outpace the ionisation rates.

The carbon-based chemistry in clouds in galaxies is therefore set by a competition between the star formation rate of the galaxy, and the density and surface density of clouds. The star formation rate controls the cosmic ray ionisation rate, as well as the ultraviolet flux. As a result, all else being equal, increased SFRs result in decreased molecular CO abundances, and increased C I and C⁺ abundances.

In order to provide the reader with some intuition as to how these effects drive carbon-based chemistry, in Figures 2 - 3, we show the CO and C⁺ abundances for a grid of model cloud densities and surface densities given a range of star formation rates (and FUV fluxes and cosmic ray ionisation rates that scale, accordingly). Note that these cloud models are principally for the purposes of the illustration

of dominant physical effects, and therefore have not been constructed via the methods in Section 2 (meaning that the SFR, Σ_{SFR} , densities and surface densities are not all interconnected, nor is there a multiphase breakdown of these clouds; they are of a single ISM phase). The effects of increased cosmic ray fluxes and FUV radiation field strengths via increased SFR on the carbon-based chemistry is clear. At low star formation rates, even relatively low n_H and Σ_H gas is sufficiently well-shielded that the carbon can exist in molecular (CO) form. Consequently, C⁺ is confined to the most diffuse gas at low SFRs. At higher SFRs the situation is reversed. Increased χ_{FUV} and cosmic ray ionisation rates dissociate CO and ionise C, thereby increasing C⁺ abundances in clouds with a large range in physical conditions. C⁺ is destroyed, and C I and CO are most efficiently formed, when the volume density and surface density of the cloud simultaneously increase.

The numerical experiments represented in Figures 2 - 3 give some intuition as to how carbon will behave in different physical environments. In the remainder of this paper, we build upon this by combining this with our model for clouds in galaxies developed in Section 2.

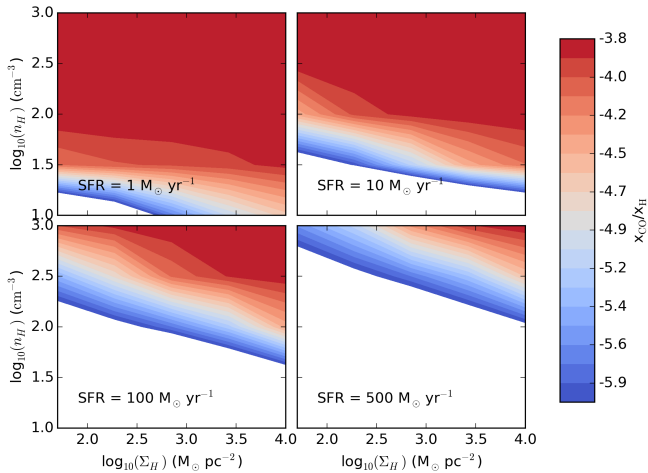


Figure 2. ^{12}CO abundance contours as a function of the volumetric and gas surface densities. Abundance contours are shown for four fiducial star formation rates, which control the far ultraviolet flux and the cosmic ray ionisation rates. At low radiation field strengths/cosmic ray ionisation rates, nearly all of the carbon is in the form of CO. At higher SFRs, UV radiation and cosmic ray ionisations contribute to the destruction of CO, especially at low densities and surface densities. The whitespace in the contour subplots denotes abundances below $10^{-6}/\text{H}_2$.

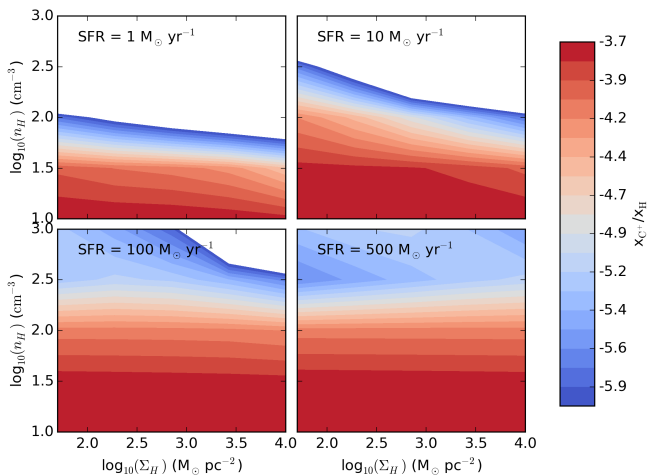


Figure 3. Similar to Figure 2, but C^+ abundance contours as a function of gas surface density and volumetric density. C^+ abundances are increased in low volume density and surface density gas, and in high ultraviolet radiation fields and/or cosmic ray fluxes. The whitespace in the contour subplots denotes abundances below $10^{-6}/\text{H}_2$.

3.2 Application to Multiphase Clouds

We are now in a place to understand the fractional abundances of carbon in its different phases in giant clouds. In Figure 4, we present the radial fractional abundances for a variety of relevant species in our chemical reaction networks

for three clouds of increasing surface density for a galaxy with gas mass $10^9 M_\odot$. These clouds are created within the context of the physical models developed in Section 2.1, and therefore have increased star formation rates (and UV fluxes/cosmic ray ionisations) with increasing cloud surface density.

For low surface density clouds, the hydrogen toward the outer most layers of the clouds is in atomic form. In these low surface density layers, photodissociation destroys H_2 , forming a photodissociated region (PDR) layer. At increasing cloud depths and surface densities, shielding by both gas and dust protects the gas from photodissociation, and hydrogen can transition from atomic to molecular phase via grain-assisted reactions.

The carbon chemistry follows a similar broad trend as the hydrogen chemistry – C^+ dominates in the outer PDR layers of the cloud, and CO toward the inner shielded layers – though the chemistry is different. In particular, in addition to UV radiation, cosmic rays also contribute to the destruction of CO via the production of He^+ . As a result, for low volume density and surface density clouds, C^+ can dominate the carbon budget both in the outer atomic PDR, as well as in much of the H_2 gas. Toward the cloud interior, the increased volume and surface densities within the cloud protect against the photodissociation/ionisation of C I and CH_x/OH_x molecules (that are principle reactants in forming CO), as well as against the production of He^+ , which is a dominant destroyer of CO (Bisbas et al. 2015). Hence, in the innermost regions of clouds where the surface densities are highest, the carbon is principally in molecular CO form.

As the total column density of a cloud increases, the transition layer between atomic and molecular (both for hydrogen and carbon) is forced to shallower radii. This occurs because, although increasing column density raises the SFR and thus the UV and cosmic ray intensities, this is outweighed by the increase in cloud shielding and volume density that accompany a rise in Σ_g . The net effect is that clouds with high surface density and thus high star formation rate also tend to be dominated by CO, with only a small fraction of their carbon in the form of C^+ .

3.3 The [C II]-FIR Relation

We are now in a position to compare our full model to the observed [C II]-FIR relation. We do so in Figure 5, using a large range of galaxy gas masses in our model, chosen to be representative of the typical gas mass range of both local galaxies and high- z galaxies (Saintonge et al. 2011; Bothwell et al. 2013; Casey et al. 2014). We compare these model tracks to observational data from both low-redshift galaxies (grey points), as well as $z > 2$ galaxies (red triangles). We discuss the local deficit relation here, and defer discussion of the high- z data to § 4.2. The local data is comprised of a compilation by Brauer et al. (2008), as well as more recent $z \sim 0$ data taken by Díaz-Santos et al. (2013) and Farrah et al. (2013). Two trends are immediately evident from Figure 5: (1) at fixed FIR luminosity, the [C II]/FIR ratio increases at larger galaxy gas mass, and (2) at increasing FIR luminosity, the [C II]/FIR ratio decreases. We discuss these trends in turn.

The trend with galaxy gas mass is straight forward to understand. The total star formation rate is an increasing

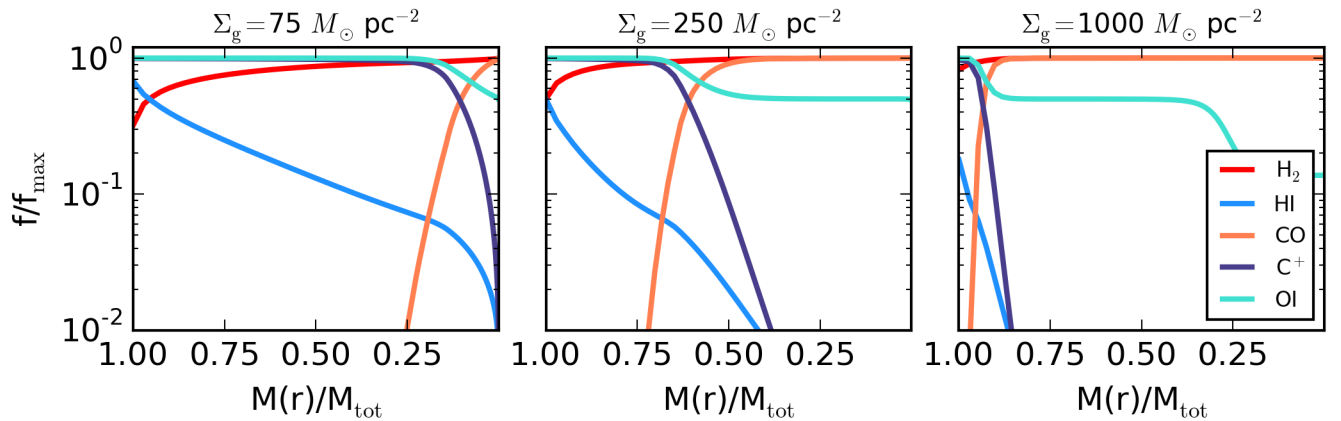


Figure 4. Radial variation of atomic and molecular abundances in three model clouds in a galaxy of $M_{\text{gas}} = 10^9 M_{\odot}$. The abundances are plotted against the Lagrangian mass enclosed such that a value of $M(r)/M_{\text{tot}} = 1$ corresponds to the surface of the cloud. Abundances are normalised to their maximum possible value, and plotted as a function of cloud radius. We show three clouds of increasing gas surface density. In general terms, the H_2 abundances increase toward the interior of clouds as shielding protects molecules from photodissociation. The carbon transitions from C^+ to CO , with the C^+ predominantly residing in the atomic PDRs and outer shell of H_2 gas. Clouds of increasing surface density have an increasing fraction of their gas in molecular H_2 form, and increasing fraction of their carbon locked in CO molecules. The oxygen abundances decrease toward the interior of clouds as the atom becomes locked up in CO and, in the inner parts of the highest surface density case, OH_x molecules.

function of both gas mass and gas surface density. Thus an increase in gas mass at fixed SFR corresponds to a decrease in Σ_g . Because Σ_g is a primary variable controlling the chemical balance between C^+ and CO , this in turn leads to an increase in the C^+ abundance. The net effect is that, at fixed SFR (and hence FIR luminosity), higher gas mass galaxies have stronger $[\text{C II}]$ emission.

The second broad trend, the decrease in the $[\text{C II}]$ -FIR ratio with increasing FIR luminosity, is the so-called $[\text{C II}]$ -FIR deficit. The origin of this is evident from examining the trends in both the gas physical properties and chemical abundances in the ISM calculated thus far (e.g. Figure 4). C^+ dominates the weakly-shielded PDR layers of giant clouds in the ISM, while CO principally resides in the well-shielded cloud interiors. Thus an increase in Σ_g drives a decrease in the amount of C^+ and an increase in the amount of CO . At the same time, an increase in Σ_g drives an increase in SFR and thus in FIR luminosity. Thus an increase in Σ_g leads to a sharp fall in the ratio of $[\text{C II}]$ /FIR. In an actual sample of galaxies the ratio of $[\text{C II}]$ to FIR falls only shallowly with FIR, however, because the dependence on Σ_g is partly offset by the dependence on gas mass. That is, galaxies with higher FIR luminosities tend to have both higher gas surface densities and higher gas masses than galaxies with lower FIR luminosities. The former drives the $[\text{C II}]$ luminosity down and the latter drives it up, but the surface density dependence is stronger (due to the exponential nature of FUV attenuation), leading to an overall net decrease in $[\text{C II}]$ emission with FIR luminosity in the observed $z \sim 0$ sample.

4 DISCUSSION

4.1 Calorimetry of Giant Clouds

Nominally, $[\text{C II}]$ line cooling is one of the principle coolants of the neutral interstellar medium. Because the $[\text{C II}]$ line emission does not increase in proportion to the star formation rate, it is interesting to consider where the cooling occurs in place of the $[\text{C II}]$ line.

In Figure 6, we revisit the cooling rates originally presented in Figure 1. For clarity, we omit the heating rates, but additionally show the cooling rates from a subset of the individual CO and $[\text{O I}]$ emission lines. As the cloud surface densities increase, the cooling rate of $[\text{C II}]$ decreases dramatically. This owes principally to the plummeting C^+ abundances. At the same time, the dominant line cooling transitions to $[\text{O I}]$ and CO . The increase in CO line cooling in part due to the rapid increase in CO abundance as the increased cloud surface density protects the molecule from photodissociation, and increased volume density combats dissociation via He^+ . The CO cooling is dominated by mid to high-J CO emission lines, with the power shifting to higher rotational transitions at higher gas surface densities (e.g., Narayanan & Krumholz 2014).

Alongside CO , line emission from $[\text{O I}]$ is an important contributor at high cloud surface densities. To see why, consider again the radial abundances within a sample cloud presented in Figure 4. Here, we now highlight the $[\text{O I}]$ abundance gradients. While the fractional $[\text{O I}]$ abundance decreases modestly with increasing gas surface density owing to increased molecule production (mostly CO and OH_x), $[\text{O I}]$ remains relatively pervasive in both atomic and molecular gas. This is to be contrasted with ionised C^+ , which tends to reside principally in the atomic PDRs of clouds,

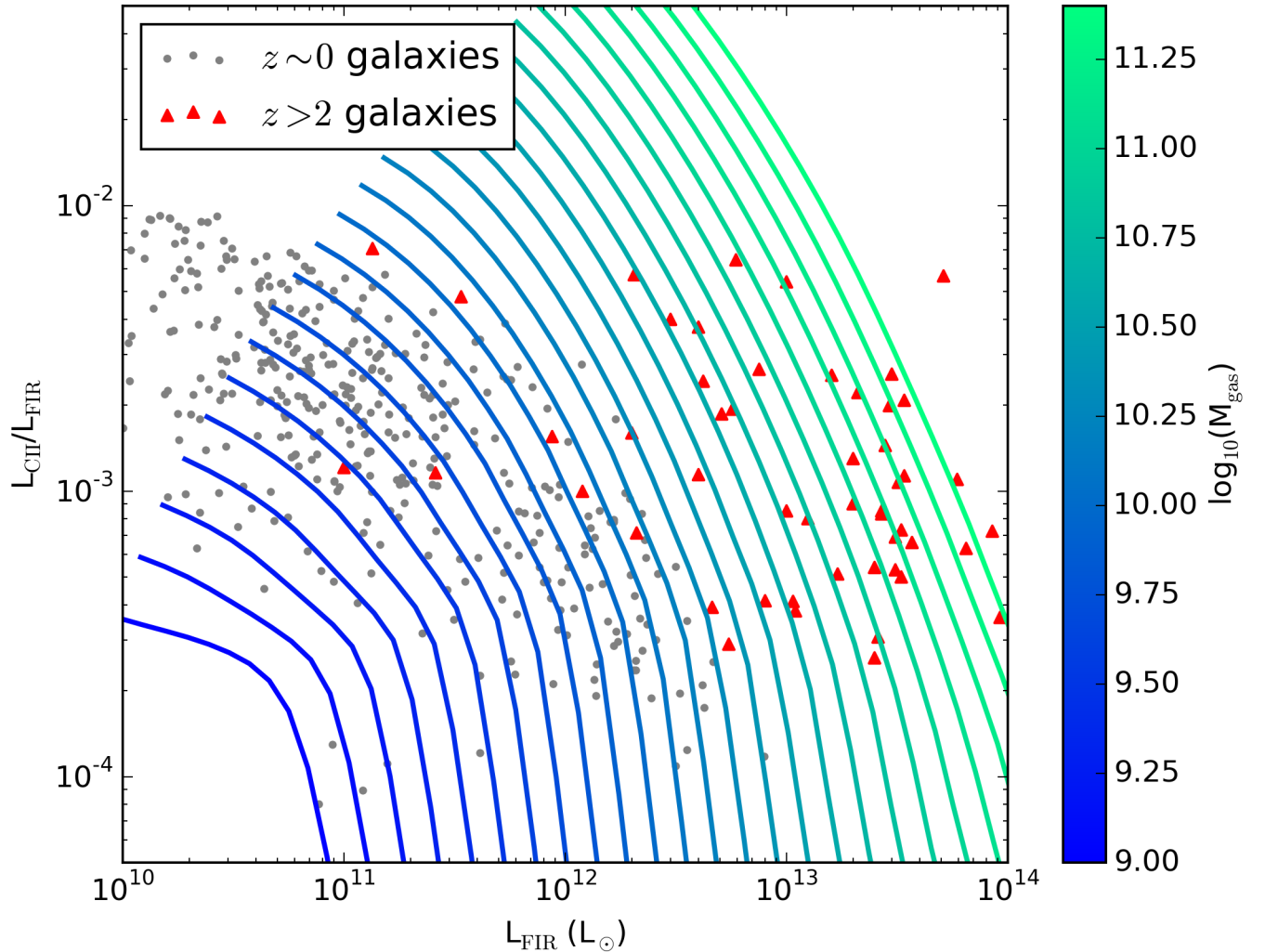


Figure 5. Theoretical [C II] luminosities (normalised by the FIR luminosity) as a function of FIR luminosity. The model tracks show predictions for galaxy gas masses $\log_{10}(M_{\text{gas}}) = [9, 11.3]$. The grey points show local $z \sim 0$ data, and the red triangles show high- z data. The lowest mass model track corresponds to the left-most one. The [C II]-FIR deficit in galaxies owes principally to a decrease in PDR mass in galaxies with increasing infrared luminosity. High-redshift galaxies are observed to be systematically at a higher infrared luminosity at a given [C II]/FIR luminosity ratio as compared to low- z galaxies. In our model, this arises because galaxies at high- z have systematically larger gas masses. At a fixed star formation rate, an increased gas mass means lower cloud surface densities on average, which results in higher [C II] luminosities. High- z detections are from Cox et al. (2011); De Breuck et al. (2011); George et al. (2013); Graciá-Carpio et al. (2011); Ivison et al. (2010); Maiolino et al. (2005); Rawle et al. (2013); Stacey et al. (2010); Swinbank et al. (2012); Valtchanov et al. (2011); Venemans et al. (2012); Wagg et al. (2012); Wang et al. (2013); Willott et al. (2013); Diaz-Santos et al. (2015); Schaerer et al. (2015); Gullberg et al. (2015).

and sometimes the outer layer of the H_2 core. So, while the mass fraction of H_2 to H I gas increases with increasing surface density clouds, [O I] remains an efficient coolant. The bulk of the cooling occurs via the [O I] 1-0 transition, though emission from the 2-1 [O I] line can be non negligible at the highest gas surface densities.

The contribution of [O I] line emission to the total cooling constitutes a prediction of our model. We quantify this in Figure 7, where we show the [C II]/[O I] luminosity ratio for our model compared to observations by Graciá-Carpio et al.

(2011) and Farrah et al. (2013) of $z \sim 0.1 - 0.3$ galaxies. The [O I] observations are of the sum of the $63 \mu\text{m}$ and $145 \mu\text{m}$ line luminosities. At high cloud surface densities, the model luminosity ratio between [C II] and [O I] decreases. Whether such a trend exists in the data is unclear, and requires additional data (especially at the high-luminosity end).

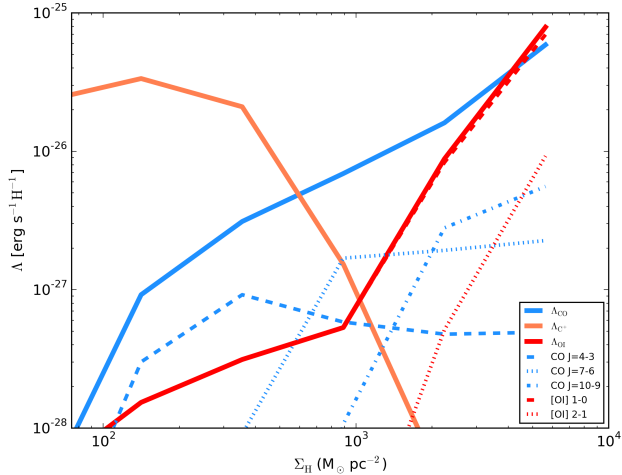


Figure 6. Cooling rates of individual lines as a function of cloud surface density for a model galaxy of mass $M_{\text{gas}} = 10^9 M_{\odot}$. As the [C II] luminosities decrease with increasing gas surface density, the principle cooling transitions to CO and [O I] emission lines. At high surface densities, the CO cooling is dominated by high-J rotational transitions. Note, because we only show a subset of the CO lines for clarity, the sum of the cooling rates of the shown CO lines won't add up to the total CO cooling rate shown.

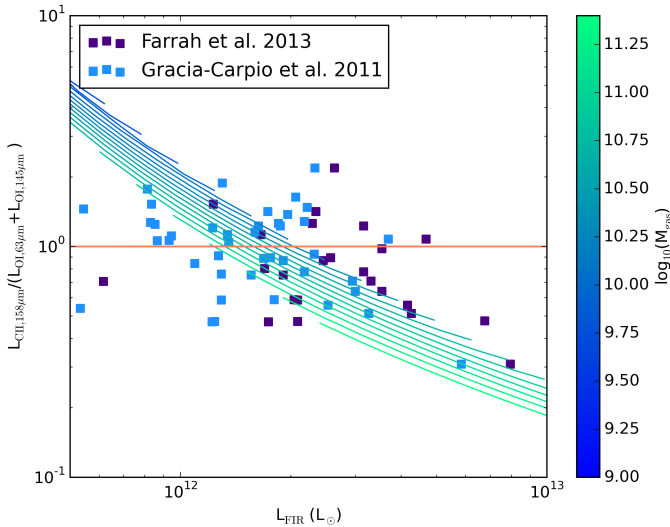


Figure 7. [C II]/[O I] cooling rates for model compared to data from Graciá-Carpio et al. (2011) and Farrah et al. (2013). The [O I] cooling rates are a sum of the $63\mu\text{m}$ and $145\mu\text{m}$ emission lines. At high gas surface density (or galaxy infrared luminosity), the dominant cooling in the model transitions from [C II] line emission to [O I] and CO line emission. The orange line shows where the cooling power transitions from [C II] to [O I].

4.2 Application to High-Redshift Galaxies

Recent years have seen a large increase in the number of [C II] detections from heavily star-forming galaxies at $z \gtrsim 2$ (e.g., Hailey-Dunsheath et al. 2008; Stacey et al. 2010; Brisbin et al. 2015; Gullberg et al. 2015; Schaerer et al. 2015), extending to the epoch of reionisation (e.g., Riechers et al. 2013; Rawle et al. 2014; Wang et al. 2013; Capak et al. 2015). Returning to Figure 5, we now highlight the high-redshift compilation denoted by the red triangles. The compilation is principally culled from the Casey et al. (2014) review article, with some more recent detections. We exclude data that have upper limits on either [C II] or FIR emission. It is clear that the high- z data are offset from low- z galaxies such that at a fixed [C II]/FIR luminosity ratio, $z \sim 2-6$ galaxies have a larger infrared luminosity. One possible interpretation of the high- z data is that the high- z galaxies exhibit a [C II]-FIR deficit akin to that observed in local galaxies, but shifted to higher luminosities.

We now highlight the model tracks overlaid for galaxies of mass between $M_{\text{gas}} = 10^{10} - 10^{11.3} M_{\odot}$. These gas masses are chosen based on the range of H_2 gas masses constrained for a sample of high- z submillimetre galaxies by (Bothwell et al. 2013). As is evident from Figure 5, the model tracks for galaxies with large gas mass show good correspondence with the observed high- z data points. This suggests that the ultimate reason for the offset in infrared luminosity for the [C II]-FIR deficit of high- z galaxies is their large gas masses. High infrared luminosity-galaxies at $z \sim 0$ typically have high star formation rates due to large values of Σ_g , but those at high- z have high star formation rates due to large gas masses instead.

Our interpretation for the offset in infrared luminosity in the high- z [C II]-FIR deficit is consistent with a growing body of evidence that, at a fixed stellar mass, galaxies at high-redshift have higher star formation rates and gas masses than those at $z \sim 0$ (Davé et al. 2010; Geach et al. 2011; Rodighiero et al. 2011; Madau & Dickinson 2014; Narayanan et al. 2012b, 2015), and that it is these elevated gas masses that are driving the extreme star formation rates, rather than a short-lived starburst event. As an example, the most infrared-luminous galaxies at $z \sim 0$ have small emitting areas (~ 1 kpc), and large measured gas surface densities, up to $\sim 10^3 M_{\odot} \text{pc}^{-2}$ averaged over the emitting area. In contrast, galaxies of comparable luminosity at high- z have a diverse range of sizes, with some gas spatial extents observed ~ 20 kpc (Casey et al. 2014; Ivison et al. 2011; Simpson et al. 2015). Indeed, cosmological zoom simulations by Narayanan et al. (2015) have shown that the extreme star formation rates of the most infrared-luminous galaxies $L_{\text{IR}} \sim 10^{13} L_{\odot}$ at $z \sim 2$ can be driven principally by significant reservoirs of extended gas at a moderate surface density. Similarly, at lower luminosities at $z \sim 2$, Elbaz et al. (2011) find that the cold dust SEDs of main sequence galaxies are consistent with more extended star formation at lower surface densities than their low- z counterparts. Our model suggests that the offset in the [C II]-FIR relation between $z \sim 0$ and $z \sim 2$ galaxies can ultimately be traced to the same phenomenon.

4.3 Relationship to other Theoretical Models

There has been significant attention paid to modeling [C II] emission from galaxies over the past 5-10 years. The methods are broad, and range from numerical models of clouds, as in this paper, to semi-analytic dark matter only simulations to full cosmological hydrodynamic calculations. Generally, models have fallen into three camps (with some overlap): (1) Models that study the [C II]-SFR relationship in low luminosity galaxies at a given redshift (e.g., [Olsen et al. 2015](#)); (2) models predicting [C II] emission from epoch of reionisation galaxies ([Nagamine et al. 2006](#); [Muñoz & Furlanetto 2013b,a](#); [Vallini et al. 2013, 2015](#); [Pallottini et al. 2015](#)); and (3) models that aim to understand the [C II]-FIR deficit in luminous galaxies. We focus on comparing to other theoretical models in this last category as they pertain most directly to the presented work here.

[Abel et al. \(2009\)](#) use CLOUDY H II region models ([Ferland et al. 2013](#)) to explore the idea, first posited by [Luhman et al. \(2003a\)](#), that [C II] emission is suppressed in high-SFR galaxies because H II regions become dust-bounded rather than ionisation bounded. In their model, this reduces the [C II] luminosity because ionising photons absorbed by dust are not available to ionise carbon. This model implicitly assumes that [C II] emission arises predominantly from ionised regions and the PDRs that surround them, because it does not consider [C II] emission coming from phases of the ISM that are not associated with the immediate environments of stellar clusters young enough to drive H II regions. However, observations suggest that H II regions and PDRs account for only $\sim 50\%$ of the [C II] emission in the Milky Way, with that fraction declining at higher SFRs ([Pineda et al. 2014](#), their Figure 6 in particular). Thus it is unclear if a model based around H II regions is capable of explaining the galaxy-averaged [C II]-FIR relation, which is dominated by other ISM phases.

[Bisbas et al. \(2015\)](#) developed cloud models with similar underlying methods to those presented here, based on the 3D-PDR code. They use their models to investigate the chemistry of CO, and find, as we do, that at high star formation rates He⁺ destruction of CO becomes an important process in determining the overall carbon chemical balance in a galaxy. However, they do not consider [C II] emission or its relationship with star formation rates. Similarly, [Popping et al. \(2013\)](#) developed semi-analytic galaxy formation models (SAMs) coupled with PDR modeling to model CO, C I and [C II] emission from model galaxies. The models provide a reasonable match to the observed $z \sim 0$ [C II]-FIR deficit, but the authors do not discuss the physical origin of the effect, nor its redshift dependence.

Finally, [Muñoz & Oh \(2015\)](#) posited an analytic model in which [C II] line saturation may drive the observed [C II]/FIR luminosity deficit. At very high temperatures ($T_{\text{gas}} \gg T_{\text{[CII]}}$), the line luminosity no longer increases with temperature, and they suggest that this phenomenon is why [C II] stops increasing with SFR at high SFRs. However, our models suggest that the gas temperatures typically do not reach such high values, at least up to $L_{\text{FIR}} \sim 10^{13}$. For example, turning to [Figure 1](#), we find maximum⁵ gas temperatures of ~ 50 K at luminosities of $L_{\text{FIR}} = 10^{13} L_{\odot}$. Further

bolstering this claim, [Narayanan et al. \(2011b\)](#) ran idealised hydrodynamic galaxy merger simulations with thermal balance models similar to the ones presented in this paper, though with the increased sophistication of directly modeling the dust temperature via 3D dust radiative transfer calculations. [Narayanan et al. \(2011b\)](#) found that even for clouds in merger-driven starbursts that exceed $\Sigma_{\text{H}_2} > 10^4 M_{\odot} \text{pc}^{-2}$, the gas kinetic temperature remained $T_{\text{kin}} \sim 10^2$ K. Thus, within the context of the thermal balance equations presented in this work, we conclude that line saturation is not likely to dominate the [C II]/FIR luminosity deficit at high infrared luminosities.

4.4 Relationship to Observations

There are a few observational works in recent years that discuss particular aspects of the [C II]/FIR luminosity deficit with FIR luminosity that are worth discussing within the context of the model that we present in this paper. In early work, [Stacey et al. \(1991\)](#) utilised PDR models to interpret their KAO observations of a sample of nearby gas-rich galaxies. These authors found that single-component PDR models did not fit their observed [C II]/FIR luminosity ratios, and posited a two-component model in which the bulk of the FIR emission arises from a confined region exposed to a high intensity UV field, while the [C II] line emission mostly comes from a more diffuse extended component exposed to a lower radiation field. This is compatible with the model we present here. While in our model we assume for simplicity that a given galaxy is comprised of a single population of clouds, in reality a galaxy will have a distribution of cloud surface densities, likely with the high Σ_{g} clouds toward the central regions associated with more active star formation. In this scenario, the FIR luminosity would predominantly arise from the high Σ_{g} clouds, while the lower Σ_{g} clouds would produce more [C II] line emission, consistent with the model developed by [Stacey et al. \(1991\)](#).

[Díaz-Santos et al. \(2013\)](#) presented Herschel observations of 241 nearby galaxies, and confirmed the [C II]-FIR deficit in their relatively large sample. They find that the luminous infrared galaxies (LIRGs) with higher infrared luminosity surface density tend to have lower [C II]/FIR luminosity ratios compared to more extended systems. Within the context of our model, we interpret this result as higher infrared luminosity density galaxies corresponding to higher gas surface density galaxies ([Kennicutt & Evans 2012](#)). Galaxies with higher gas surface densities will have lower atomic PDR masses with respect to their H₂ molecular masses, and therefore lower [C II] luminosities.

4.5 Uncertainties in the Model

While we aim to provide a relatively minimalist analytic model for the structure of giant clouds in galaxies in [Section 2](#), there are a number of free parameters that we had to choose that can impact the overall normalisation of the [C II]/FIR ratio in our model galaxies. In this section, we explore the impact of these parameters on our results. In

mass. Functionally, we find a maximum temperature of $T \sim 100$ K for our most massive galaxies.

⁵ This number of course increases with increasing galaxy gas

Figure 8, we summarise the impact of varying the star formation law index (N), the density normalisation (ρ_{MW}), and the cosmic ray ionisation rate (ζ_{-16}).

All of these values are uncertain. Star formation indices ranging from sublinear to quadratic have been reported in the literature (Kennicutt & Evans 2012). Decreasing the star formation law index decreases the average density of our model clouds which has a two-fold effect. First, it decreases the total star formation rate via longer cloud free fall times. Second, [C II] is more easily formed owing to decreased recombination and molecular formation rates. Increasing the cloud density normalisation (ρ_{MW}) has the opposite effect.

Similarly, the cosmic ray ionisation rate in galaxies is uncertain. Observations of H_3^+ within the Galaxy suggest rates that range from $\zeta_{-16} \approx 0.1 - 3$ (McCall et al. 1999; Indriolo et al. 2007; Neufeld et al. 2010; Wolfire et al. 2010). For lack of a better constraint, we have chosen to employ a relatively conservative value ($\zeta_{-16} = 0.1 \times \text{SFR}/(\text{M}_\odot \text{ yr}^{-1})$), noting that increased cosmic ray ionisation rates tend to result in more [C II] flux. This is shown explicitly in Figure 8, where we test a model with $\zeta_{-16} = 3 \times \text{SFR}/(\text{M}_\odot \text{ yr}^{-1})$.

For all of these tested variations in our parameter choice survey, the overall trend is similar: the [C II]/FIR luminosity ratio decreases with increasing galaxy star formation rate. This is because the net decrease in the [C II]/FIR luminosity ratio owes to decreasing relative PDR masses in increasingly luminous galaxies in our model. The normalisation and exact behaviour of course depends on uncertain parameters, but the broad trends are robust.

Finally, we note that the linear scaling of the cosmic ray ionisation rate with star formation rate is rooted in the tentative observational evidence for such a scaling by Abdo et al. (2010). However, it is plausible that the cosmic ray ionisation rate scales with some other parameter, such as star formation rate density or surface density. We defer a more thorough investigation into the chemical consequences of varying ionisation rate scalings to a forthcoming study.

5 SUMMARY

We have developed models for the physical structure of star-forming giant clouds in galaxies, in which clouds consist of both atomic and molecular hydrogen. We coupled these cloud models with chemical equilibrium networks and radiative transfer models in order to derive the radial chemical and thermal properties, and utilised these models to investigate the origin of the [C II]/FIR luminosity deficit in luminous galaxies. Our main results follow:

(i) The carbon-based chemistry in clouds can be reduced to a competition between volumetric density and surface density protecting the formation of molecules against cosmic-ray induced ionisations, and UV photodissociations/ionisations.

(ii) At solar metallicities, the molecular H_2 core in clouds tends to be well-shielded from UV radiation, and dense enough to combat CO destruction by cosmic rays (via an intermediary He^+ reaction) as well as ultraviolet radiation. As a result, the carbon in molecular gas is principally in the form of CO. This said, the lower surface density surfaces of the central molecular core can contain significant amounts of C^+ .

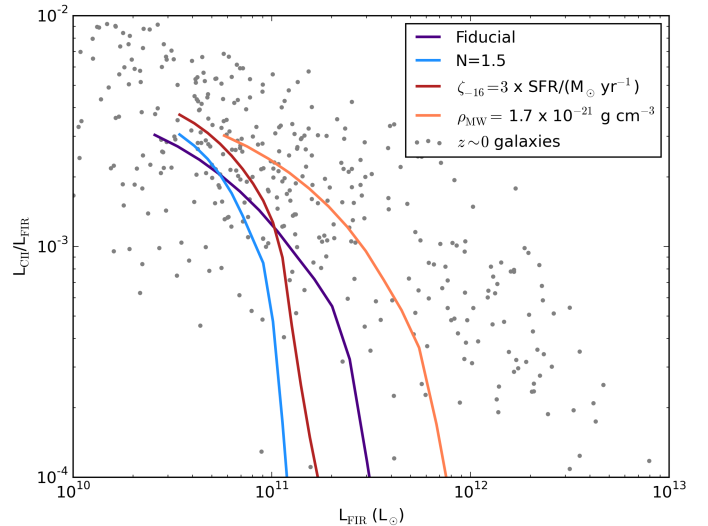


Figure 8. [C II]/FIR luminosity ratio versus FIR luminosity for our fiducial model (thick blue), and three varying parameters in our cloud models. The example shown is for a $M_{\text{gas}} = 3 \times 10^9 \text{M}_\odot$ galaxy, the average mass (in log-space) of our low-redshift galaxy mass range. See Table 1 for variable definitions.

(iii) The opposite is true for atomic PDRs. The carbon in the PDR shell in clouds is easily exposed to the radiation and cosmic ray field, resulting in the bulk of carbon being in ionised C^+ form.

(iv) At increasing galaxy star formation rate (and infrared luminosity), the typical cloud surface density (Σ_{g}) rises; with increasing Σ_{g} , the molecular fraction ($\text{H}_2/\text{H I}$) rises, and the relative [C II] luminosity decreases owing to a shrinking of the size of the [C II] emitting region. These reduced PDR masses in increasingly luminous galaxies are the fundamental origin of the [C II]/FIR luminosity deficit with FIR luminosity in galaxies in our model.

(v) As the [C II] luminosity decreases in high surface density clouds, the major coolants of the ISM transition to high-J CO emission lines and [O I].

(vi) At a fixed star formation rate, galaxies of increasing gas mass have lower cloud surface densities, and hence larger [C II] luminosities. Because of this, galaxies at high-redshift, which have larger gas fractions than their low- z counterparts, lie offset from low- z galaxies in [C II]-FIR space. Our model provides a natural explanation for the offset [C II]-FIR deficit for high- z galaxies.

ACKNOWLEDGEMENTS

The authors thank Thomas Bisbas, Tanio Diaz-Santos, Duncan Farrah, and Munan Gong, Javier Gracia-Carpio and Eve Ostriker for providing both simulation and observational data that aided us when developing these models. D.N. thanks Aaron Evans, Thomas Greve, Rob Kennicutt, Dominik Riechers, J.D. Smith, Gordon Stacey, Dan Stark, and Karen Olsen for helpful conversations. Partial support for DN was provided by NSF AST-1009452, AST-1442650, NASA HST AR-13906.001 from the Space Tele-

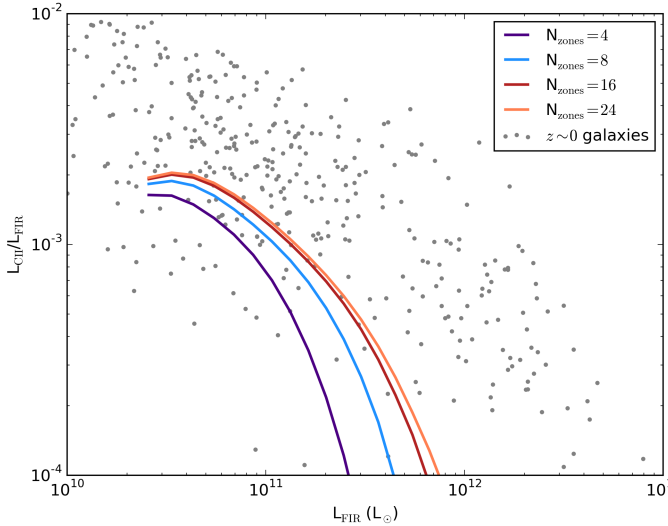


Figure A1. Convergence test for number of radial zones in model clouds. Test shows model [C II]-FIR deficit for a galaxy of mass $M_{\text{gas}} = 3 \times 10^9 M_{\odot}$, the average mass (in log-space) of our low-redshift galaxy mass range.

scope Science Institute, which is operated by the Association of University for Research in Astronomy, Incorporated, under NASA Contract NAS5-26555, and a Cottrell College Science Award, awarded by the Research Corporation for Science Advancement. MRK acknowledges support from US NSF grant AST-1405962 and Australian Research Council grant DP160100695.

APPENDIX A: RESOLUTION TESTS

Our fiducial model clouds are subdivided into 16 radial zones. In Figure A1, we test the convergence properties of this model by varying the number of zones from 4-24 for a model galaxy of $\log(M_{\text{gas}}) = 9.5 M_{\odot}$. While differences exist at the lowest [C II] luminosities between $N_{\text{zone}} = 16$ and $N_{\text{zone}} = 24$, they are minor.

References

Abdo A. A., et al., 2010, *ApJ*, **709**, L152
 Abel N. P., Dudley C., Fischer J., Satyapal S., van Hoof P. A. M., 2009, *ApJ*, **701**, 1147
 Abrahamsson E., Krems R. V., Dalgarno A., 2007, *ApJ*, **654**, 1171
 Barinova Ğ., van Hemert M. C., Krems R., Dalgarno A., 2005, *ApJ*, **620**, 537
 Beirão P., et al., 2010, *A&A*, **518**, L60
 Bertoldi F., McKee C. F., 1992, *ApJ*, **395**, 140
 Bigiel F., Leroy A., Walter F., Brinks E., de Blok W. J. G., Madore B., Thornley M. D., 2008, *AJ*, **136**, 2846
 Bisbas T. G., Papadopoulos P. P., Viti S., 2015, *ApJ*, **803**, 37
 Blanc G. A., Heiderman A., Gebhardt K., Evans II N. J., Adams J., 2009, *ApJ*, **704**, 842
 Bolatto A. D., Leroy A. K., Rosolowsky E., Walter F., Blitz L., 2008, *ApJ*, **686**, 948
 Boselli A., Lequeux J., Gavazzi G., 2002, *AP&SS*, **281**, 127

Bothwell M. S., et al., 2013, *MNRAS*, **429**, 3047
 Braucher J. R., Dale D. A., Helou G., 2008, *ApJS*, **178**, 280
 Brisbin D., Ferkinhoff C., Nikola T., Parshley S., Stacey G. J., Spoon H., Hailey-Dunsheath S., Verma A., 2015, *ApJ*, **799**, 13
 Capak P. L., et al., 2015, *Nature*, **522**, 455
 Casey C. M., Narayanan D., Cooray A., 2014, *Physics Reports*, **541**, 45
 Chomiuk L., Povich M. S., 2011, *AJ*, **142**, 197
 Cox P., et al., 2011, *ApJ*, **740**, 63
 Croxall K. V., et al., 2012, *ApJ*, **747**, 81
 Davé R., Finlator K., Oppenheimer B. D., Fardal M., Katz N., Kereš D., Weinberg D. H., 2010, *MNRAS*, **404**, 1355
 De Breuck C., Maiolino R., Caselli P., Coppin K., Hailey-Dunsheath S., Nagao T., 2011, *A&A*, **530**, L8
 Díaz-Santos T., et al., 2013, *ApJ*, **774**, 68
 Díaz-Santos T., et al., 2015, preprint, ([arXiv:1511.04079](https://arxiv.org/abs/1511.04079))
 Dobbs C. L., Burkert A., Pringle J. E., 2011, [arXiv:1101.3414](https://arxiv.org/abs/1101.3414)
 Dobbs C. L., et al., 2013, in Beuther H., Klessen R. S., Dullemond C. P., Henning T., eds, *Protostars and Planets VI*. University of Arizona Press
 Dobbs C. L., et al., 2014, *Protostars and Planets VI*, pp 3–26
 Draine B. T., 2011, *Physics of the Interstellar and Intergalactic Medium*. Princeton University Press: Princeton, NJ
 Draine B. T., Bertoldi F., 1996, *ApJ*, **468**, 269
 Elbaz D., et al., 2011, *A&A*, **533**, A119
 Farrah D., et al., 2013, [arXiv:1308.4165](https://arxiv.org/abs/1308.4165),
 Ferland G. J., et al., 2013, *RMXAA*, **49**, 137
 Geach J. E., Smail I., Moran S. M., MacArthur L. A., Lagos C. d. P., Edge A. C., 2011, *ApJ*, **730**, L19
 George R. D., et al., 2013, *MNRAS*, **436**, L99
 Glover S. C. O., Clark P. C., 2012, *MNRAS*, **421**, 116
 Glover S. C. O., Mac Low M.-M., 2007, *ApJS*, **169**, 239
 Glover S. C. O., Mac Low M.-M., 2011, *MNRAS*, **412**, 337
 Goldsmith P. F., 2001, *ApJ*, **557**, 736
 Goldsmith P. F., Langer W. D., Pineda J. L., Velusamy T., 2012, *ApJS*, **203**, 13
 Graciá-Carpio J., et al., 2011, *ApJ*, **728**, L7
 Gullberg B., et al., 2015, *MNRAS*, **449**, 2883
 Hailey-Dunsheath S., Nikola T., Oberst T., Parshley S., Stacey G. J., Farrah D., Benford D. J., Staguhn J., 2008, in Kramer C., Aalto S., Simon R., eds, *EAS Publications Series Vol. 31*, *EAS Publications Series*. pp 159–162, [doi:10.1051/eas:0831031](https://doi.org/10.1051/eas:0831031)
 Herrera-Camus R., et al., 2015, *ApJ*, **800**, 1
 Heyer M., Dame T. M., 2015, *ARA&A*, **53**, 583
 Indriolo N., Geballe T. R., Oka T., McCall B. J., 2007, *ApJ*, **671**, 1736
 Indriolo N., Neufeld D. A., Gerin M., Geballe T. R., Black J. H., Menten K. M., Goicoechea J. R., 2012, *ApJ*, **758**, 83
 Iono D., et al., 2006, *ApJ*, **645**, L97
 Ivison R. J., et al., 2010, *A&A*, **518**, L35
 Ivison R. J., Papadopoulos P. P., Smail I., Greve T. R., Thomson A. P., Xilouris E. M., Chapman S. C., 2011, *MNRAS*, **412**, 1913
 Jaquet R., Staemmler V., Smith M. D., Flower D. R., 1992, *Journal of Physics B Atomic Molecular Physics*, **25**, 285
 Kennicutt R. C., Evans N. J., 2012, *ARA&A*, **50**, 531
 Krumholz M. R., 2012, *ApJ*, **759**, 9
 Krumholz M. R., 2013a, *MNRAS*,
 Krumholz M. R., 2013b, DESPOTIC: Derive the Energetics and Spectra of Optically Thick Interstellar Clouds, Astrophysics Source Code Library ([ascl:1304.007](https://ascl.net/1304.007))
 Krumholz M. R., 2014, *Phys. Rep.*, **539**, 49
 Krumholz M. R., Tan J. C., 2007, *ApJ*, **654**, 304
 Krumholz M. R., McKee C. F., Tumlinson J., 2008, *ApJ*, **689**, 865
 Krumholz M. R., McKee C. F., Tumlinson J., 2009a, *ApJ*, **693**, 216

- Krumholz M. R., McKee C. F., Tumlinson J., 2009b, *ApJ*, **699**, 850
- Krumholz M. R., Leroy A. K., McKee C. F., 2011, *ApJ*, **731**, 25
- Krumholz M. R., Dekel A., McKee C. F., 2012, *ApJ*, **745**, 69
- Launay J.-M., Roueff E., 1977, *Journal of Physics B Atomic Molecular Physics*, **10**, 879
- Leech K. J., et al., 1999, *MNRAS*, **310**, 317
- Leroy A. K., et al., 2013, *AJ*, **146**, 19
- Lique F., Werfelli G., Halvick P., Stoecklin T., Faure A., Wiesenfeld L., Dagdigan P. J., 2013, *J. Chem. Phys.*, **138**, 204314
- Luhman M. L., et al., 1998, *ApJ*, **504**, L11
- Luhman K. L., Briceño C., Stauffer J. R., Hartmann L., Barrado y Navascués D., Caldwell N., 2003a, *ApJ*, **590**, 348
- Luhman M. L., Satyapal S., Fischer J., Wolfire M. G., Sturm E., Dudley C. C., Lutz D., Genzel R., 2003b, *ApJ*, **594**, 758
- Madau P., Dickinson M., 2014, *ARA&A*, **52**, 415
- Maiolino R., et al., 2005, *A&A*, **440**, L51
- Malhotra S., et al., 1997, *ApJ*, **491**, L27
- Malhotra S., et al., 2001, *ApJ*, **561**, 766
- McCall B. J., Geballe T. R., Hinkle K. H., Oka T., 1999, *ApJ*, **522**, 338
- McKee C. F., Krumholz M. R., 2010, *ApJ*, **709**, 308
- Muñoz J. A., Furlanetto S. R., 2013a, arXiv/1309.6636,
- Muñoz J. A., Furlanetto S. R., 2013b, *MNRAS*, **435**, 2676
- Muñoz J. A., Oh S. P., 2015, preprint, (arXiv:1510.00397)
- Murphy E. J., et al., 2011, *ApJ*, **737**, 67
- Nagamine K., Wolfe A. M., Hernquist L., 2006, *ApJ*, **647**, 60
- Narayanan D., Davé R., 2012, *MNRAS*, **423**, 3601
- Narayanan D., Krumholz M. R., 2014, *MNRAS*, **442**, 1411
- Narayanan D., Cox T. J., Hayward C. C., Hernquist L., 2011a, *MNRAS*, **412**, 287
- Narayanan D., Krumholz M., Ostriker E. C., Hernquist L., 2011b, *MNRAS*, **418**, 664
- Narayanan D., Krumholz M. R., Ostriker E. C., Hernquist L., 2012a, *MNRAS*, **421**, 3127
- Narayanan D., Bothwell M., Davé R., 2012b, *MNRAS*, **426**, 1178
- Narayanan D., et al., 2015, *Nature*, **525**, 496
- Nelson R. P., Langer W. D., 1999, *ApJ*, **524**, 923
- Neufeld D. A., et al., 2010, *A&A*, **521**, L10
- Nikola T., Genzel R., Herrmann F., Madden S. C., Poglitsch A., Geis N., Townes C. H., Stacey G. J., 1998, *ApJ*, **504**, 749
- Olsen K. P., Greve T. R., Narayanan D., Thompson R., Toft S., Brinch C., 2015, preprint, (arXiv:1507.00362)
- Osterbrock D. E., Ferland G. J., 2006, *Astrophysics of gaseous nebulae and active galactic nuclei*. University Science Books: Sausalito, CA
- Pallottini A., Gallerani S., Ferrara A., Yue B., Vallini L., Maiolino R., Feruglio C., 2015, *MNRAS*, **453**, 1898
- Papadopoulos P. P., 2010, *ApJ*, **720**, 226
- Pineda J. L., Langer W. D., Goldsmith P. F., 2014, *A&A*, **570**, A121
- Popping G., Pérez-Beaupuits J. P., Spaans M., Trager S. C., Somerville R. S., 2013, arXiv/1310.1476,
- Rawle T. D., et al., 2013, arXiv/1310.4090,
- Rawle T. D., et al., 2014, *ApJ*, **783**, 59
- Riechers D. A., et al., 2013, *Nature*, **496**, 329
- Rigopoulou D., et al., 2014, *ApJ*, **781**, L15
- Robitaille T. P., Whitney B. A., 2010, *ApJ*, **710**, L11
- Rodighiero G., et al., 2011, *ApJ*, **739**, L40
- Saintonge A., et al., 2011, *MNRAS*, **415**, 32
- Sargsyan L., et al., 2012, *ApJ*, **755**, 171
- Schaerer D., et al., 2015, *A&A*, **576**, L2
- Schöier F. L., van der Tak F. F. S., van Dishoeck E. F., Black J. H., 2005, *A&A*, **432**, 369
- Schroder K., Staemmler V., Smith M. D., Flower D. R., Jaquet R., 1991, *Journal of Physics B Atomic Molecular Physics*, **24**, 2487
- Shetty R., Kelly B. C., Rahman N., Bigiel F., Bolatto A. D., Clark P. C., Klessen R. S., Konstandin L. K., 2013a, *MNRAS*,
- Shetty R., Kelly B. C., Bigiel F., 2013b, *MNRAS*, **430**, 288
- Simpson J. M., et al., 2015, *ApJ*, **799**, 81
- Stacey G. J., Geis N., Genzel R., Lugten J. B., Poglitsch A., Sternberg A., Townes C. H., 1991, *ApJ*, **373**, 423
- Stacey G. J., Hailey-Dunsheath S., Ferkinhoff C., Nikola T., Parshley S. C., Benford D. J., Staguhn J. G., Fiolet N., 2010, *ApJ*, **724**, 957
- Staemmler V., Flower D. R., 1991, *Journal of Physics B Atomic Molecular Physics*, **24**, 2343
- Swinbank A. M., et al., 2012, *MNRAS*, **427**, 1066
- Vallini L., Gallerani S., Ferrara A., Baek S., 2013, *MNRAS*, **433**, 1567
- Vallini L., Gallerani S., Ferrara A., Pallottini A., Yue B., 2015, arXiv/1507.00340,
- Valtchanov I., et al., 2011, *MNRAS*, **415**, 3473
- Venemans B. P., et al., 2012, *ApJ*, **751**, L25
- Wagg J., et al., 2012, *ApJ*, **752**, L30
- Wang R., et al., 2013, *ApJ*, **773**, 44
- Wiesenfeld L., Goldsmith P. F., 2014, *ApJ*, **780**, 183
- Willott C. J., Omont A., Bergeron J., 2013, *ApJ*, **770**, 13
- Wolfire M. G., McKee C. F., Hollenbach D., Tielens A. G. G. M., 2003, *ApJ*, **587**, 278
- Wolfire M. G., Hollenbach D., McKee C. F., 2010, *ApJ*, **716**, 1191
- Yang B., Stancil P. C., Balakrishnan N., Forrey R. C., 2010, *ApJ*, **718**, 1062
- de Looze I., Baes M., Bendo G. J., Cortese L., Fritz J., 2011, *MNRAS*, **416**, 2712
- van Dishoeck E. F., Black J. H., 1988, *ApJ*, **334**, 771